Memory Seeds Enable High Structural Phase Purity in 2D Perovskite Films for High-Efficiency Devices

Siraj Sidhik, Wenbin Li, Mohammad Samani, Hao Zhang, Yafei Wang, Justin Hoffman, Austin Fehr, Michael Wong, Claudine Katan, Jacky Even, et al.

https://doi.org/10.1002/adma.202007176
Sidhik S et al. Adv. Mater. 33, 29, 2007176 (2021)

Memory seeds enable high structural phase purity in 2D perovskite films for high-efficiency devices

Siraj Sidhik, Wenbin Li, Mohammad H. K. Samani, Hao Zhang, Yafei Wang, Justin Hoffman, Austin K. Fehr, Michael Wong, Claudine Katan, Jacky Even, Amanda B. Marciel, Mercouri G. Kanatzidis, Jean-Christophe Blancon and Aditya D. Mohite**

Dr. S. Sidhik, W. Li, M. H. K. Samani, H. Zhang, Y. Wang, A. K. Fehr, M. Wong, A. B. Marciel
Dr. J.-C. Blancon, Dr. A. D. Mohite Department of Chemical and Biomolecular Engineering,
Rice University
Houston, Texas 77005, USA
Email : blanonjc@gmail.com, adm4@rice.edu

W. Li, H. Zhang
Applied Physics Graduate Program,
Smalley- Curl Institute
Rice University
Houston, Texas, 77005, USA

J. Hoffman, Prof. M. G. Kanatzidis
Department of Chemistry and Department of Materials Science and Engineering,
Northwestern University
Evanston, Illinois 60208, USA

Dr. C. Katan
Univ Rennes, ENSCR, INSA Rennes, CNRS,
ISCR (Institut des Sciences Chimiques de Rennes) - UMR 6226,
F-35000 Rennes, France.

Prof. J. Even
Univ Rennes, INSA Rennes, CNRS
Institut FOTON, UMR 6082
Rennes F-35000, France

Keywords: two- dimensional perovskite, intermediate phase, crystallinity, orientation, photostability

Two-dimensional (2D) perovskites are a class of halide perovskites offering a pathway for realizing efficient and durable optoelectronic devices. However, the broad chemical phase space and lack of understanding of film formation have led to quasi-2D perovskite films with polydispersity in perovskite layer thicknesses, which have hindered devices performance and

stability. Here, we demonstrate a simple and scalable approach termed as the phase-selective method to fabricate 2D perovskite thin-films with high phase purity. The phase-selective method involves dissolution of single-crystalline powders with homogeneous perovskite layer thickness in desired solvents to fabricate thin-films. In-situ characterizations reveal the presence of sub-micron-sized seeds in solution that preserve the memory of the dissolved single-crystals and dictate the nucleation and growth of grains with identical thickness of the perovskite layers in thin-films. Photovoltaic device with a p-i-n architecture were fabricated with such films, which yield an efficiency of 17.1% enabled by an open-circuit voltage of 1.20V, while preserving 97.5% of their peak-performance after 800 hours under illumination without any external thermal management.

Low-dimensional materials have offered tremendous promise due to the novel properties arising from their size and structure. However, preserving their pristine properties when they are solution-processed to form thin films or hierarchical assemblies required for applications has been major bottleneck across multiple fields and materials for several decades[1–6]. For example, when assembled into thin films, the unique properties of low-dimensional materials realized at a single crystal level are overshadowed due to disorder arising from materials polydispersity (heterogeneity in size, structure, and orientation), which results in inefficient charge and energy transport in optoelectronic devices. This is largely because there is a limited understanding of the particle growth, crystallization, and solvation dynamics, which dictate long-range ordering and properties of low-dimensional material based thin films. Recently, organic-inorganic 2D perovskites have emerged as a new family of 2D semiconductors with unique and tunable physical properties that can be preserved in bulk single crystals.[7–15] However, and despite encouraging proof-of-concept thin-film devices,[16–22] polydispersity or mixed crystal phases leads typically to a high density of structural phase impurities in films,[17,23,24] which has limited device performance and prevented access to specific 2D physical properties in these films.[11,15,25]

The 2D perovskites synthesized in this work consist of nanometer-thick layers of organic-inorganic halide perovskite with the formula $A'_2A_{n-1}M_nX_{3n+1}$ (where A is a small organic cation, M is a metal, X is a halide, and *n* defines the layer thickness) that are separated one from another by layers of large A' organic cations.[26,27] A key challenge is to design a reliable, generally applicable and scalable process to synthesize phase-pure 2D perovskite thin-films dominantly formed by a homogeneous distribution of a single perovskite layer thickness, and with a perovskite layer thickness intermediate between the 2D perovskite *n*=1 and the 3D perovskite limiting cases.[25,28,29] However, the classical synthesis method typically yields a mixture of *n*-phase and 3D perovskites.[24] There have been recent attempts to realize thin-films with narrow distribution of *n*-value 2D perovskites by using different solvents and organic additives that control the crystallization kinetics. Unfortunately, these efforts have had limited success, and do not generalize to all types of 2D perovskites.[30–33] Our previously reported hot casting method seems to yield better phase purity in thin films for a few types of 2D perovskites, yet there is little understanding of the intermediate chemical steps in the films formation, which has limited the dissemination of this method to other 2D perovskites.[34] We anticipate that the discovery of a reliable synthesis method to fabricate phase pure 2D perovskite thin films will enable optoelectronic devices that concomitantly exhibit high efficiency, scalability, long-term operational stability, as well as pave the path for new types of devices, which exploit the rich physics of 2D materials. Indeed, studying films that are made of multiple phases frustrates our ability to understand the properties of the 2D perovskites. However, overcoming this long-standing and serious bottleneck mandates a deep understanding of the genesis of phase purity during thin-film formation, with the desired control over orientation and crystallinity.

Here, we report on a phase-selective synthesis method involving a pre-crystallization step of 2D perovskite crystalline powders followed by single-step solution processing, to produce 2D perovskite thin-films principally formed from perovskite layers with a single-valued layer thickness (or *n*-value), with good crystallinity and desired orientation suitable for fabricating optoelectronic devices. Comprehensive in-situ X-ray diffraction and correlated in-situ absorbance measurements with dynamic light scattering (DLS) analysis reveals the exact nature of 2D perovskite film formation where the growth is dominated by the nucleation of 200 nm homogeneous *n*-value seeds. Proof-of-concept photovoltaic measurements performed on the phase-pure 2D perovskite films exhibit an efficiency of 17.1%, which arises from an increase in the open circuit voltage (V_{OC}) and fill factor (FF) as expected from a film with a homogenous energy landscape (or band-gap).

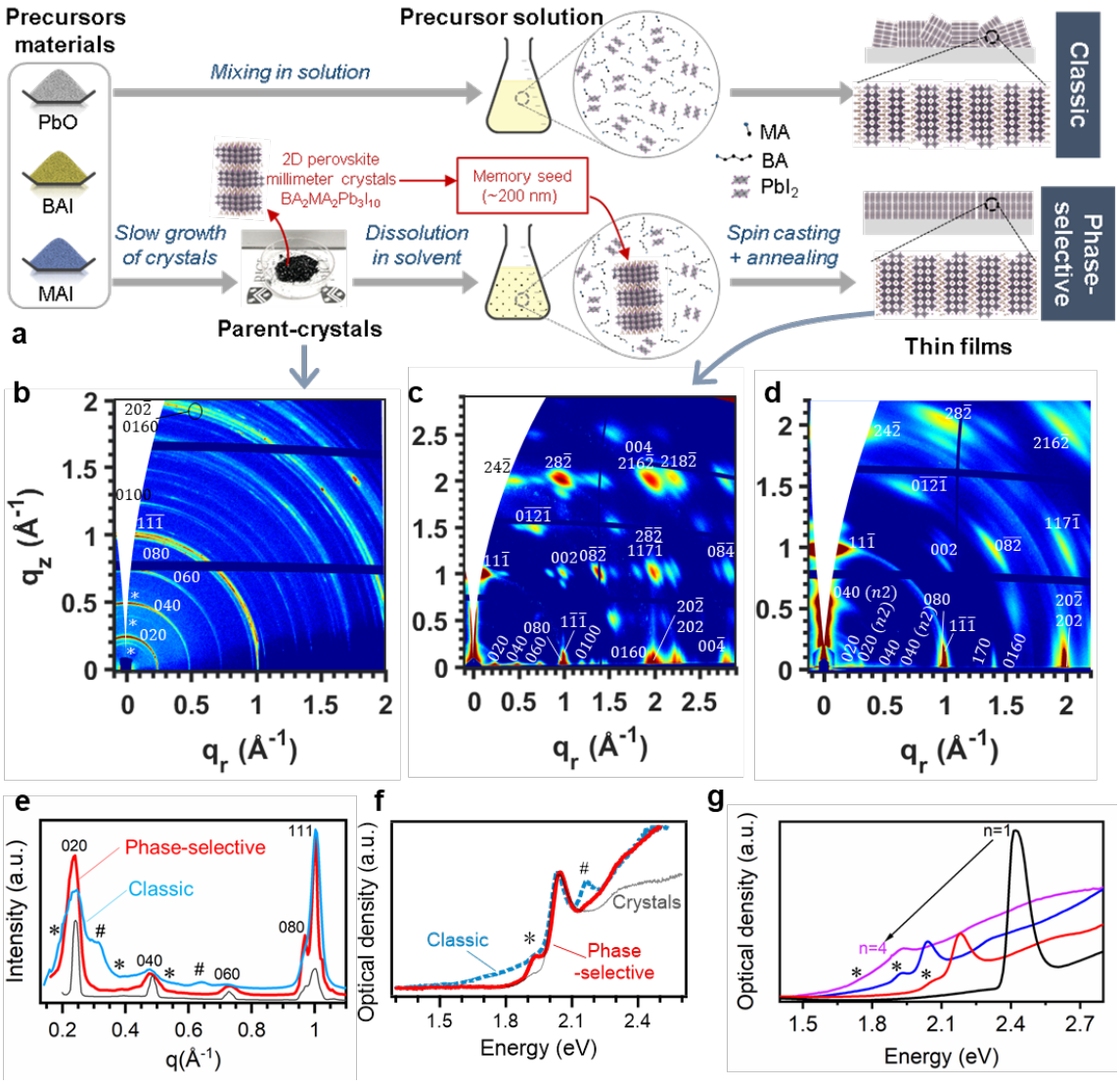

Fig. 1 a) Sketch of the phase-selective synthesis method from this work and the classic synthesis method already reported in the literature. Example of the Ruddlesden-Popper $BA_2MA_2Pb_3I_{10}$ 2D perovskites here. Grazing incidence wide-angle x-ray scattering patterns of b) the parent-crystal powders, c) the thin films synthetized with the phase-selective method and d) the classically synthetized thin films. Labels indicate the Miller indices of the principal diffraction peaks derived from the simulated diffraction pattern of the thin films with convention and plane directions (see details in Fig. S2 and S3). e) Angular-integrated diffraction patterns of the thin films prepared with the phase-selective and classic synthesis methods, and comparison to the parent-crystals. f) Corresponding optical absorbance spectra. Here, the star and hash symbols identify the *n*=4 and *n*=2 impurity phases. g) Optical absorbance spectra of the Ruddlesden-popper thin film *n=1-4* fabricated by phase selective strategy. Here the star symbol identifies the corresponding *n+1* impurity phase.

Fig. 1 illustrates the two methods used to fabricate thin films of 2D perovskites – the classical one-step and our approach termed as "phase-selective" method employed for fabricating thin-films of 2D perovskites and the corresponding structural and optical properties of the films. The classic synthesis method involves dissolving (by stirring for 12 hours) precursor materials (for example, PbI_2, BAI, and MAI, with BA and MA standing for butylammonium and methylammonium, respectively) in stoichiometric proportions corresponding to the desired *n*-value in solution, followed by spin casting on a substrate and annealing at 100°C.[24] This approach yields thin-films with a mixture of 2D perovskite *n*-phase materials. For example, when precursors are mixed in stoichiometric proportions to fabricate $BA_2MA_2Pb_3I_{10}$ (*i.e.* Ruddlesden-Popper *n*=3 2D perovskite), the classic synthesis method produces films composed of a mixture of the *n*=2, *n*=3, and *n*=4 2D perovskite phases and often with evidences of the 3D halide perovskites.[24,35] These films are often referred to as quasi-2D and denoted as $\langle n \rangle$=3 films. In order to promote phase selectivity during thin-film formation, we added an extra step in the synthesis protocol. First, we slowly crystallized 2D perovskite single crystal powders (micrometer to millimeter sizes) of a desired *n*-value from the precursor materials hereafter termed as parent-crystals (Fig. 1a).[26,27] These parent crystals exhibited a high degree of phase purity, typically around 90 to 95% as validated using x-ray powder diffraction measurements. As illustrated in Fig. 1b for the $BA_2MA_2Pb_3I_{10}$ parent-crystal powders, the diffraction signal stems predominantly from the *n*=3 phase with less than 10 % of *n*=4 impurities. These parent-crystals were then dissolved by heating at 70 ℃ in the optimized solvent for 6 or more hours and the resulting solution was spin casted and annealed.

After optimization of the solvent composition (5 wt% MACl with the 2D single-crystal powder in DMF for the Ruddlesden-Popper $BA_2MA_2Pb_3I_{10}$) and dissolution process (Fig. S1), we synthesized thin-films, which exhibited a narrow variation of phase distribution in comparison to the classical method as verified by grazing incidence wide-angle x-ray scattering (GIWAXS) and absorption spectroscopy. The GIWAXS pattern of the *n*=3 Ruddlesden-Popper 2D perovskite films synthesized with the phase-selective method is shown in Fig. 1c. A spot-like diffraction pattern indicates higher crystallinity than the films fabricated using the classical method as shown in Fig. 1d. The experimental GIWAXS pattern was accurately reproduced and the diffraction peaks indexed from the 2D perovskite single crystal structure with vertically oriented perovskite layers (see the illustration of the structure and details of the analysis in the Fig. S2 and S3). The degree of phase purity observed in oriented films (Fig. 1c) was also confirmed by abrasing the thin films (see details in Fig. S4) and measuring the XRD pattern of the powder. In contrast to the results obtained in Fig. 1c using the phase selective method, similar measurements on the films produced using the classical method (Fig. 1d) resulted in mixed phases of 2D perovskite with high *n*-value and 3D perovskites, which exhibited a lower degree of crystallinity and non-preferential orientation of the perovskite layers (more ring-like pattern).[36] Fig. 1e shows the integrated diffraction intensity over all azimuthal directions of the GIWAXS patterns for the thin-films produced using the phase-selective and the classical method, which are both compared with the pattern of the parent single-crystal powders (grey curve). The phase mixing is clearly observed by the mismatch of several diffraction peaks in the classic thin films as compared to the diffraction of the parent crystals. Complimentary to the GIWAXS line cuts, we also measured the absorbance spectra of the thin-films using the two methods. The analysis of the results from GIWAXS and absorbance yields a phase purity of about 90% for the $BA_2MA_2Pb_3I_{10}$ films. One the other hand,

we estimated a distribution of n=3 and n=2 phases in equal quantity, as well as the presence of n=4 and phases with higher n-value or 3D-like perovskite (blue dashed curve in Fig. 1e, f) in the classic thin films. We note that the small values of absorbance below 1.8 eV indicates a negligible amount of high n-value crystal phases or 3D-like perovskite in our films, and we attribute this small absorption to previously observed surface states resulting from the local distortions observed in the GIWAXS data.[37–39]

Next, we verified the applicability of the phase selective approach to thin films of Ruddlesden-popper with different n thicknesses ($n=1, 2, 4$). Based on the optical absorbance of the films, we infer a phase purity 90%) of the desired n value with a few percentages of $n+1$ impurities and negligible amount of higher n-value crystal phases or 3D (see Fig. 1g). Using the Debye Scherrer analysis on the (111) diffraction peak (Fig. S5), we extracted an average size of 31 nm for the thin films. These values are comparable to those of the parent-crystals (average grain-size 64 nm), thus confirming that the crystalline quality is well preserved in the thin films made using the phase-selective method. To further check if our synthesis approach is applicable to 2D perovskite crystals with other compositions and structures, we performed measurements on the Dion Jacobson n=3 2D perovskite thin films (4AMP-$MA_2Pb_3I_{10}$ where 4AMP is 4- Amino methyl piperidine, Fig. S6-S8), which also demonstrated results consistent with those obtained for Ruddlesden-Popper thin-films.

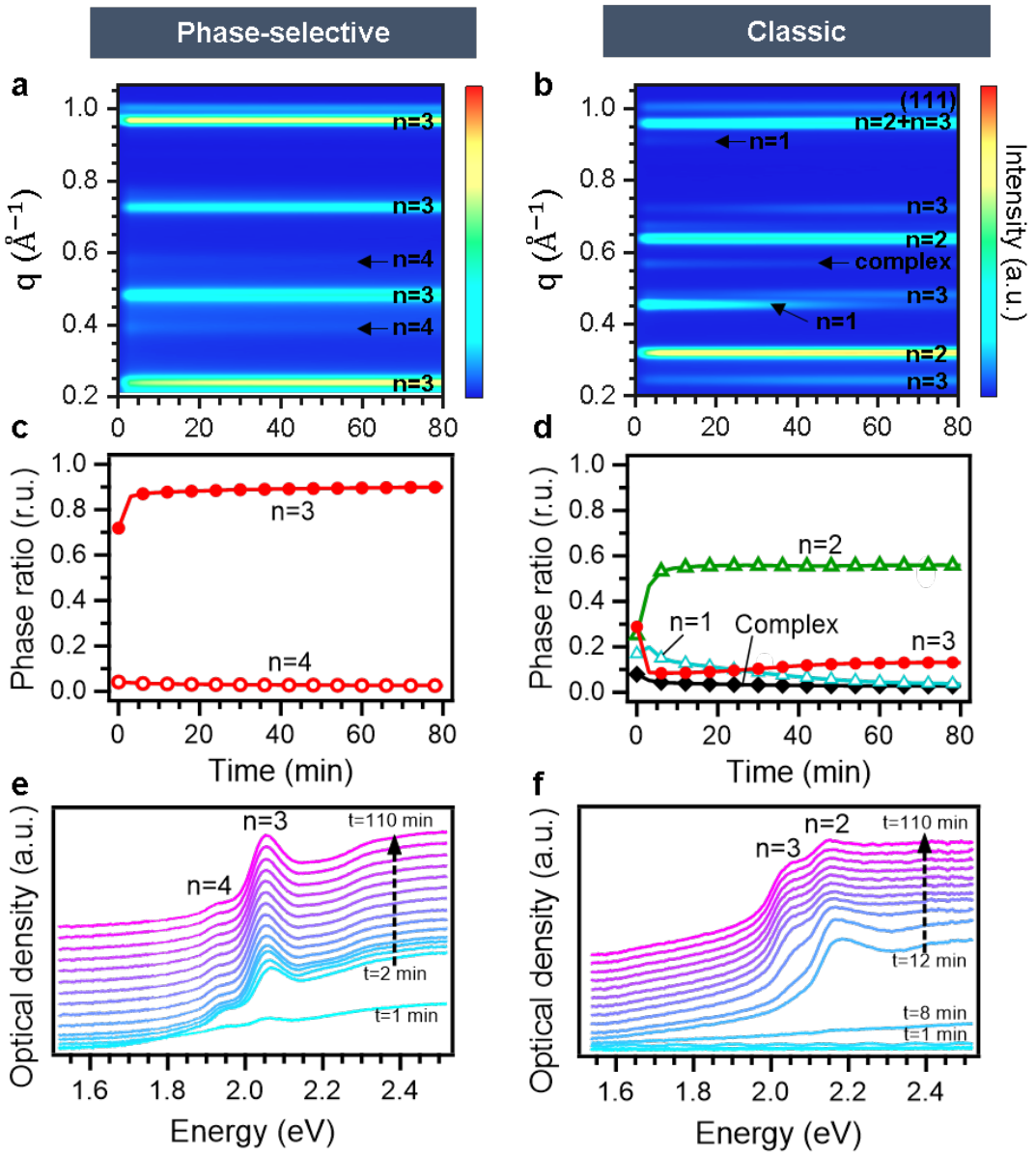

Fig. 2 a, b) Evolution of the x-ray diffraction during film formation and comparison between our phase-selective synthesis method and the classic one. All peaks were identified to a 2D perovskite phase of defined *n*-value (or perovskite layer thickness), except for one peak assigned to the presence of an intermediate complex in solution. c, d) Corresponding evolution of the ratio of each phase relative to the fully integrated diffraction. e, f) Evolution of the optical absorbance spectra of the films during synthesis. Each peak in the spectra correspond to the ground exciton transition of a given perovskite layer thickness.

The significant differences in the degree of phase purity and crystal orientation observed between the thin-films synthesized with the phase-selective and the classical method imply that the method

of preparation of the precursor solutions before casting significantly affects the kinetics of formation of the 2D perovskite thin-films. For the classic synthesis method, Quintero-Bermudez *et al.*[24] proposed a kinetic model showing that intermediate solvent complexes provide a framework for nucleation of the 2D perovskite layers during the annealing process. However, there has been no prior report on understanding the mechanism that leads to phase pure 2D perovskite films using the phase-selective method. Therefore, in order to understand the differences in the crystallization kinetics and film formation between the two synthesis methods we performed in-situ x-ray diffraction and absorbance of the thin-films during its growth, as illustrated in **Fig. 2**, which has shown to be a powerful approach for identifying the chemical origin of the different phases (*n* values) during the thin-film formation.[24] These experiments were performed by spin casting the respective precursor solution on a glass microscope slide, which was kept at room temperature without annealing in order to slow down the kinetics of nucleation and film formation. We note that this process also yielded films like those obtained by post annealing (Fig. S9). Fig. 2a and 2b illustrate the evolution of the diffraction pattern as a function of time from the moment the precursor solutions were spin casted up to eighty minutes of continuous monitoring of the x-ray diffraction pattern. The signature diffraction peaks of each 2D perovskite phase were identified and monitored as a function of time with respect to the total diffraction of the sample (Fig. 2c, d). Both methods showed diffraction at about q=1 $Å^{-1}$ after one minute, indicative of the formation of the halide perovskite film, and after a few minutes most of the solution nucleated and formed 2D perovskite phases. We also observed a weak diffraction peak in the classic method around 0.57 $Å^{-1}$, which indicates the presence of intermediate phase complexes in the excess solution.[24] Recent work on the classical synthesis method has demonstrated the existence of an intermediate gel phase during growth.[40] This gel phase was identified as one of the processes that hinders the formation

of homogenous 2D perovskite thin films. For film growths using the phase-selective method, the targeted *n*=3 2D perovskite phase formed relatively more quickly and continued growing over time as the amount of excess solution is consumed (Fig. 2a, 2c). Based on these data, we infer that the phase-selective synthesis method bypasses the intermediate phase (absence of diffraction peak corresponding to intermediate phase complex), which promotes the formation of the desired layer thickness with negligible phase segregation. The absence of intermediate phase in the phase selective method is the result of poor interaction between the solvent and the undissolved seeds. Hence, the film growth is solvent independent when compared to the classic method where the evaporation of the solvents leads to the film formation process.

In order to verify the different phases of thin-film formation, we also performed in-situ optical absorbance measurements as illustrated Fig. 2e, which corroborated that after a couple of minutes the solution nucleates dominantly into the *n*=3 2D perovskite phase. The excess solution, which is not consumed initially, allows for further improvement of the purity of the *n*=3 phase at the expense of the *n*=4. The *n*=4 impurity phase decreased to a few percent after tens of minutes, as confirmed by both x-ray diffraction and absorbance data (Fig. 2a, c, e). On the other hand, analysis of the film formation in the classic synthesis method yields a mixture of *n*=1 and *n*=2 phases after a few minutes of nucleation (Fig. 2b, d, f). Subsequently, we observed the formation of the *n*=3 2D perovskite phase over a period of tens of minutes, accompanied by the dissolution of the *n*=1 2D perovskite crystals. The final film from the classic method at the end of our experiment was composed of a mixture of *n*=2 and *n*=3 2D perovskites with little excess solution remaining. These in-situ experiments emphasize the important differences in film formation between the phase-selective method and the classic one. First, we note that in the phase-selective method, the desired 2D perovskites phase (*n*=3) is readily formed as the dominant phase from the initial nucleation of

the solution. In contrast, the classical method initially yields phases with lower *n* value, followed by a subsequent slow growth of the expected phase.[41,42] Second, the rate of nucleation is significantly faster in the phase-selective method compared to the classic approach, as validated from the absorbance data. These observations suggest that despite their apparently identical clear yellow colour and similar viscosity (Fig. S10), there exist significant differences in the solvation dynamics (precursor-solvent interactions) and the chemical origin of the two precursor solutions prepared for each synthesis method.

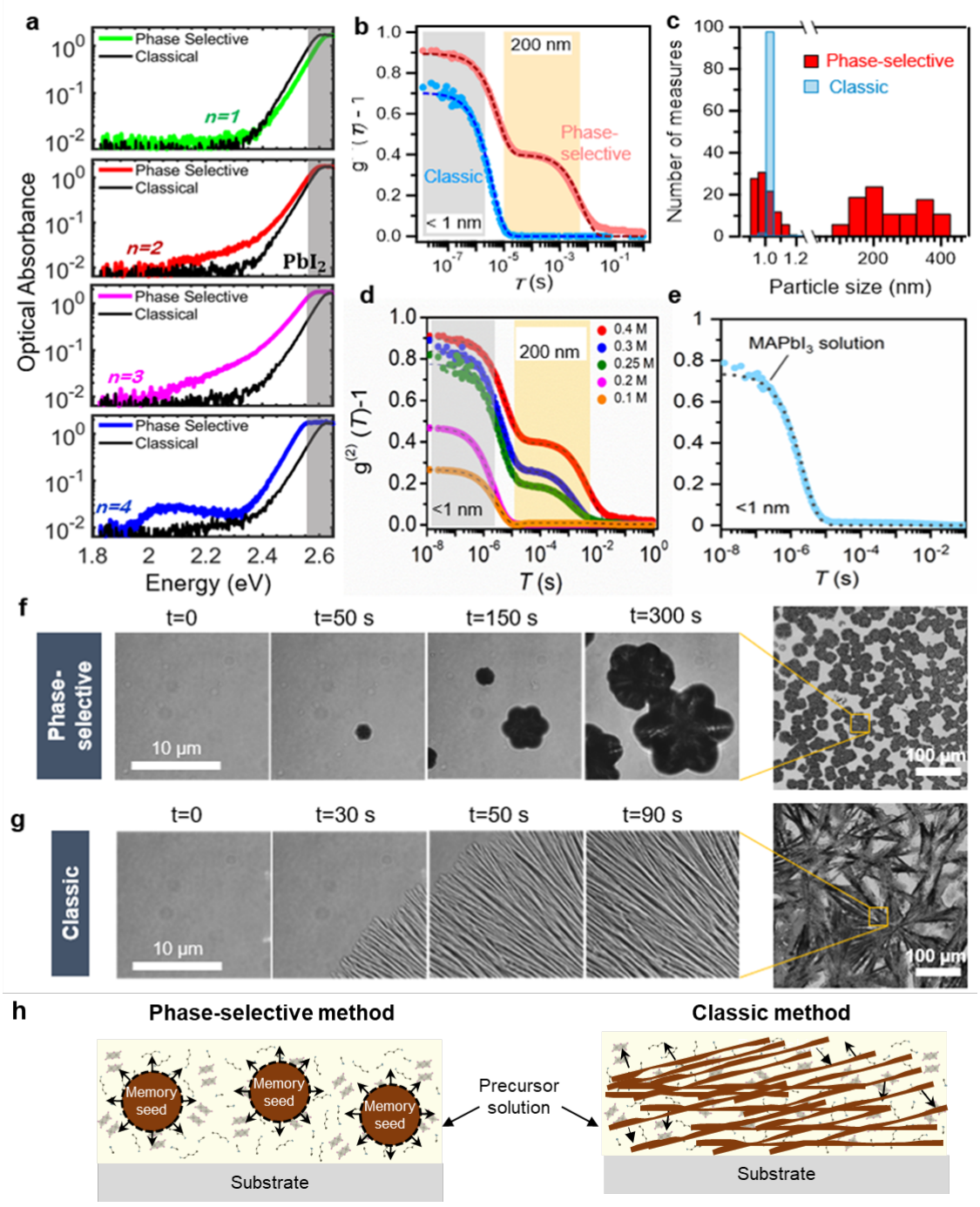

Fig. 3 a) Optical absorbance of the precursor solutions obtained before spin coating and annealing. The gray region corresponds to the absorption of PbI_2. b) Correlation function versus delay time derived from dynamic light scattering performed on the precursor solutions. c) Statistical distribution of the particle size in solution and comparison between our phase-selective synthesis method and the classic one. d) Correlation function versus delay time derived from dynamic light scattering performed for different concentration of the perovskite solution for the phase-selective method. Dashed lines are fit to the data. Gray and orange regions indicate small and large particle

size in solution, respectively, e) Correlation function versus delay time derived from dynamic light scattering performed on the $MAPbI_3$ solution obtained by dissolving the synthesized crystals in the solvent, f-g) In-situ visualization of the formation of grains in 2D perovskite thin films and comparison between the phase-selective synthesis method and the classic one, h) .

In order to elucidate the underlying mechanism that results in phase-pure films using the phase-selective method (Fig. 1), we investigated the composition of the precursor solution using correlated absorbance and dynamic light scattering measurements (**Fig. 3)**. Fig. 3a shows the optical absorbance as a function of excitation energy for the precursor solutions prepared using both the classical and phase-selective methods. The absorbance spectra measured for the solutions prepared using the classical method showed an absorbance edge of 2.4 eV (black curve in Fig. 3a) independent of the stoichiometry of the solution (n=1, 2, 3 and 4). The optical absorbance spectra is consistent with that obtained for PbI_2 ions in solution, also in agreement with the recent report of Quintero-Bermudez and co-workers.[24] On the other hand, the precursor solutions prepared using the phase-selective method yield, in addition to the PbI_2 absorbance, an absorbance edge varying from 2.1 eV for *n=2*, to 2.0 eV for *n=3*, and to 1.85 eV for *n=4*. These values match very well the optical bandgap energy observed in the corresponding parent single-crystals[43]. Since the absorption edge for the *n=1* 2D perovskite solution overlaps with the absorbance of the PbI_2, we were unable to resolve it from the solution. These absorbance measurements imply that there is a clear difference in chemical species for the precursor solutions prepared using the classical and phase-selective method.

Next, we used DLS to probe the size distribution of the chemical species in the precursor solutions. Fig. 3b shows the correlation versus time for both the classical and phase selective methods. The solutions prepared using the classical method showed a mono-modal distribution (single exponential), which when fitted using a single decay model (see details in method section

of the SI) yielded an average particle size of ~1 nm. The latter is in close agreement with the PbI_2 bond length of 0.7 nm. Therefore, based on the DLS results and the absorbance spectra, we attribute this to the presence of PbI_2 ions in chemical equilibrium with the solvent. On the other hand, the DLS measurements performed on the solution prepared using the phase selective method revealed a bimodal distribution with one similar to the classical solution with <1 nm sized particle and a much larger size distribution with an average particle size ~200 nm (red curve, Fig. 3b). These correlated DLS and the absorbance measurements presented in the previous paragraph unambiguously confirmed the presence of undissolved seeds in solution with the chemical makeup of the parent crystal dissolved for making the solution, hence termed as memory seeds.

We infer that these seeds remain in chemical equilibrium with the solvent for a given concentration. To verify this, we varied the dilution level (from 0.4M to 0.1M) of 2D perovskite crystal solution, and found a critical point (0.2 M) at which the bimodal correlation (indicative of the presence of the large sized memory seeds) changes to a unimodal correlation (similar to the precursor solution prepared using classical method), Fig. 3d. This can be attributed to the disruption of the chemical equilibrium between the seed and the solvent. Therefore, based on the dilution experiments and the absorbance data, suggests that the detected large seeds are indeed a remnant of the n=3 phase of the parent-crystals dissolved in solution. We note that the approach of dissolving single-crystalline powders in solution has been previously tested for fabricating 3D perovskite thin films with better morphology and enhanced crystalline quality.[44,45] As a control experiment, we also performed a correlated dynamic light scattering and absorption measurements on the $MAPbI_3$ solution obtained by dissolving parent crystals. We obtained a typical size of approximately 1 nm (see Fig. 3e) and absorption corresponding to PbI_2 (see Fig. S12), which is

fundamentally different from the phase selective solution obtained by dissolving the 2D perovskites.

The next logical step towards understanding the mechanism of film formation was to directly image the precursor solutions during the formation of 2D perovskite thin-films (Fig. 3f, g) using in-situ high-resolution microscopy. We noticed striking differences in the nucleation and grain formation between the two synthesis protocols. In the case of the classic method, we observed a random nucleation of 2D perovskite grains with filament-like morphology, which grow to form the film (Fig. 3g). On the other hand, in the phase-selective method each grain nucleated at a single location from the undissolved seed and grew radially outward and independently from the other grains (Fig. 3f). These grain boundaries are formed when either two grains coalesced during the growth or all reactants in solution are consumed and the growth terminates. From the scaled down in-situ microscopic image shown in Fig. 3f, we estimate a concentration of less than 10^{-10} M of active seeds in the precursor solution. The observation of nucleation and grain growth using the two protocols was captured in movies (Supplementary Movie 1 and Movie 2) and is depicted schematically in Fig. 3h. The films synthesized with the phase-selective method featured relatively large (micron size) and ordered grains, whereas the classic method yielded disordered wire-like morphology (Fig. 3f, g, right side images, and confirmed by characterization of the surface morphology of post annealed films in Fig. S13). We note that although we use the same time scale in Fig. 3f and 3g, the resulting macroscopic growth of the films was in fact faster using the phase-selective method as observed during the in-situ experiments in Fig. 2. Here, we observe a large number of grains nucleated simultaneously in the phase-selective growth, whereas in the classic synthesis method, the film growth was slower and occurred at the interfaces between nucleated crystals and solution. These results further corroborate the inferences from the absorbance and

DLS experiments, that the precursor solutions in the phase-selective method contain a low-density of undissolved seeds for the nucleation of 2D perovskite grains as illustrated in the schematic of Fig. 1a. In addition, consistent with the analysis of the in-situ experiments in Fig. 2, they show that the seeds in solution retain the memory of the phase of the 2D perovskite parent-crystals, which were dissolved to form the precursor solution for film growth in the phase-selective synthesis method.

Based on the measurements described in Fig. 2 and Fig. 3, we develop a model as illustrated in Fig. 3h, which depicts the mechanism of film formation in both types of synthesis methods. In the classical method, the nucleation initiates at the air-liquid interface and the nucleation front sweeps across the film as discussed in previous work[46,47]. In comparison, the phase-selective method the nucleation takes place preferentially at the memory seeds that create grains with high phase purity as imaged using the microscopy (see Fig. 3f). More recently it was claimed that colloids identified as MA^+/PbI_x complexes promote the nucleation of mixed *n*-phase in 2D perovskite films.[32] The needle-shaped crystal film morphology reflects the initial formation of solvated intermediates phases such as the one-dimensional non-perovskite ($CH_3NH_3PbI_3 \cdot DMF$) as has been recognized in $MAPbI_3$ film growth previously.[48] Then the final phase(s) form by subsequent reactions that accomplish the conversion. The phase-selective method avoids these solvated intermediates as the existing seeds act to grow the correct 2D phase. It is therefore apparent that the two different methods have very different starting points and end up at very different destinations during the film formation process, with the phase-selective method affording purer single-phase 2D films. Another advantage of the phase-selective method is that it facilitates a single step thin film deposition due to solvent independent seed assisted growth, thereby significantly improving film reproducibility critical for scaling-up in comparison to other

deposition strategies like anti-solvent, hot casting, and sequential deposition.[24,32,49] In addition, the concentration of the solvent can be tuned in the phase-selective method to achieve different size of the memory seeds and achieve solvent independent phase selective growth adapted to user's requirements (see Fig. S1, S3 and 3d).

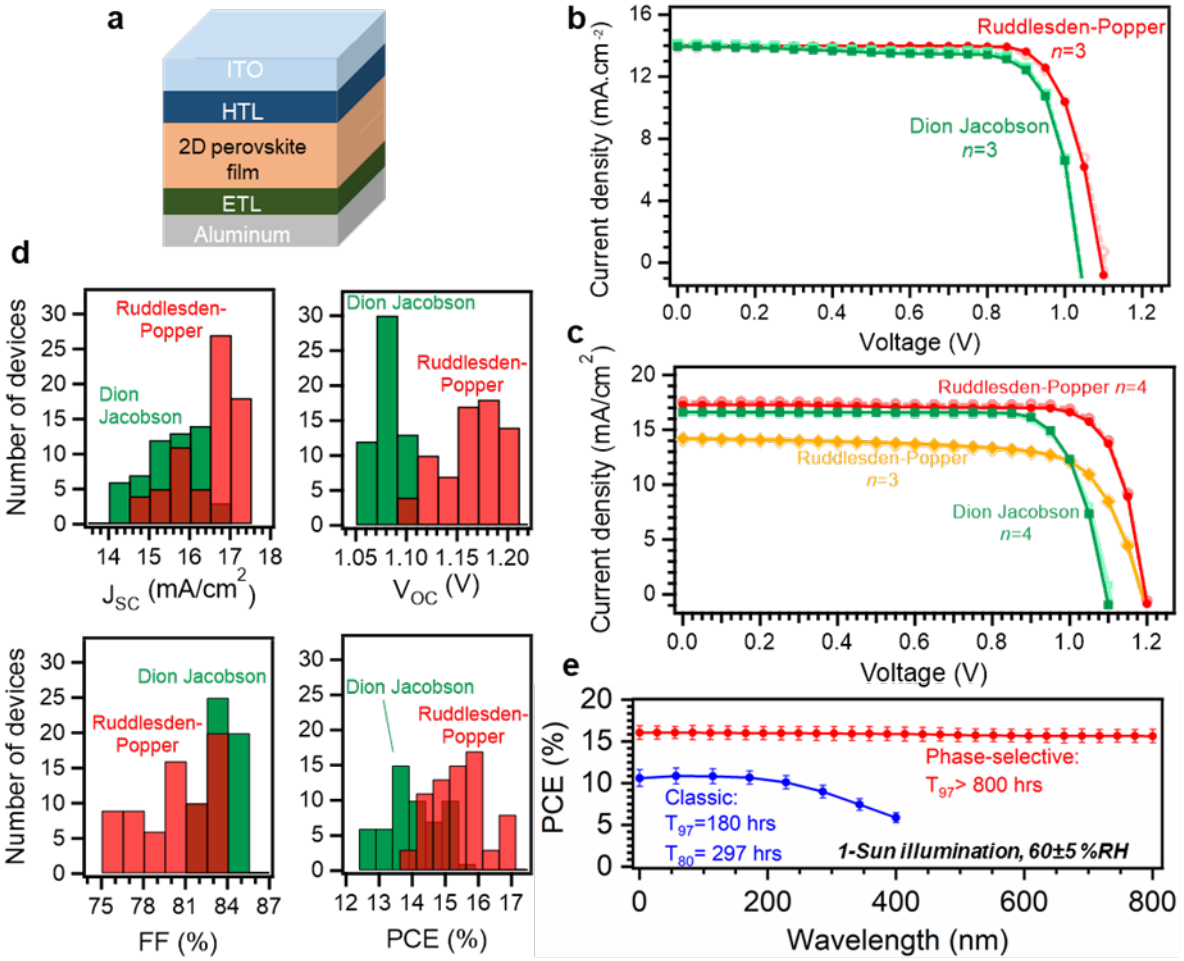

Fig. 4 a) Schematics of the solar cell devices where HTL and ETL stand for the hole and electron transporting layers. b) Current-voltage characteristics of the cells using the *n*=3 thin films of Ruddlesden-Popper (BA) and Dion Jacobson (3AMP) prepared with the phase-selective method. The HTL is PEDOT: PSS in this case. c) Current-voltage characteristics of our champion solar cells using 2D perovskite thin films of Ruddlesden-Popper (BA) with *n*=3 and *n*=4, and Dion Jacobson (3AMP) with *n*=4 synthetized with the phase-selective method. The HTL is NiOx here. Light-colored curves correspond to reverse voltage bias scans. d) Statistical distribution of the figures of merit of the *n*=4 2D perovskite solar cells shown in c, e) Statistical distribution of the stability data obtained by measuring four devices with an average efficiency (16.0±0.98%) for the

phase selective method from the same batch, for a Ruddlesden-Popper (BA) with *n*=4 solar cell under constant 1-Sun illumination and 60±5 %RH compared to the stability measured in a reference thin film solar cell with average efficiency (10.58±1.4%) fabricated with the classic method.

To illustrate the impact of phase purity of the 2D perovskite thin-films in devices, we fabricated p-i-n junction planar solar cells using the standard ITO/HTL/2D-Perovskite/ETL/Al architecture (see **Fig. 4a**). The ETL used was PCBM and two HTLs - PEDOT: PSS and NiO were used. Solar cells based on the Ruddlesden-Popper $BA_2MA_2Pb_3I_{10}$ (n=3) films prepared with the phase-selective method yielded a peak power conversion efficiency (PCE)of 12.60% with a V_{OC}= 1.1 V, J_{SC}= 14.0 mA.cm^{-2}, and fill factor (FF) of 83% with negligible hysteresis (Fig. 4b). We also tested photovoltaic devices fabricated using Dion Jacobson 4AMP-$MA_2Pb_3I_{10}$ films, which exhibited a peak PCE of 11.40% and at least 3% higher than our previous result[34]. However, it has been well established that the PCE with PEDOT:PSS as the HTL has been limited by the energy band alignment[50].

Therefore, with the goal of improving the efficiency, we fabricated photovoltaic devices using $BA_2MA_2Pb_3I_{10}$ (*n*=3), $BA_2MA_3Pb_4I_{13}$ (*n*=4), 4AMP-$MA_3Pb_4I_{13}$ (*n*=4) phase pure 2D perovskite with NiO as the HTL (Fig. 4c). The champion device was obtained using a $BA_2MA_3Pb_4I_{13}$ film, which showed a J_{SC}=17.56 mA.cm^{-2}, V_{OC}=1.20 V, fill factor 81.1%, and power conversion efficiency 17.1 %, with negligible hysteresis. The stabilized efficiency of 17.0% measured at the maximum power point (V_{OC}= 0.99V) is depicted in Fig. S14. The highest efficiency device using the Dion-Jacobson 4AMP-$MA_3Pb_4I_{13}$ film and $BA_2MA_2Pb_3I_{10}$ (*n*=3) was 15.7%, and 14.3% respectively. The statistics over tens of $BA_2MA_3Pb_4I_{13}$ and 4AMP-$MA_3Pb_4I_{13}$ devices presented in Fig. 4d confirm the reproducibility of the solar cell performances and clearly demonstrate that the phase-selective method used to synthesize the 2D perovskite thin films yields large open-circuit

voltage and fill-factor. The external quantum efficiency (EQE) and the integrated current density for the Ruddlesden-popper (n=3, and n =4) 2D perovskite solar cells is depicted in Fig. S15. The average EQE is in good agreement with the current density obtained from the J-V characteristics with <5% difference in the J_{SC} arising from a spectral mismatch between two sources. Importantly, the contribution to the EQE from the impure phases was ~9% of the J_{SC} consistent with our absorbance and GIWAX measurements in Fig. 1e and 1f. In order to understand the differences in the device performance between the classical and phase selective method, we fabricated solar cells using $BA_2MA_2Pb_3I_{10}$ (*n*=3), $BA_2MA_3Pb_4I_{13}$ (*n*=4) using classical method (see Fig. S16). The champion device using the classical method with a stoichiometric precursor composition for $BA_2MA_2Pb_3I_{10}$ (*n*=3) and $BA_2MA_3Pb_4I_{13}$ (n=4) resulted in a PCE of 9.3% and 11.0% respectively (see S16C for statistics). The photovoltaic parameters of the $BA_2MA_2Pb_3I_{10}$ (*n*=3), and $BA_2MA_3Pb_4I_{13}$ (*n*=4) 2D perovskite solar cells fabricated using the phase-selective and classical method is tabulated in Table S1.

The values obtained for the power conversion efficiency are among the best compared to previous results based on <n> quasi-2D perovskite solar cells.[18,22,42,51–55] We note that although the use of quasi-2D perovskite films is beneficial for achieving current densities larger than 20 $mA.cm^{-2}$ as compared to about 17 $mA.cm^{-2}$ here with high phase purity films, it actually limits the V_{OC} and FF. The use of quasi-2D perovskite films indeed allows enhancing near-infrared absorption as compared to the lower values observed in high phase purity films (Fig. 1g and Fig. S15) and achieves a balance between photoexcited electron-hole pair (or exciton) dissociation and material stability, however recent studies have demonstrated that a combination of the device field and low-density surface states can efficiently achieve exciton dissociation in 2D perovskite phases with low *n*-value.[25,37,56] By achieving high phase purity with the phase-selective method, 2D

perovskite thin films naturally exhibit less structural defects, related to the polydispersity of classical films, which for example might result in stacking faults and dangling bonds between two adjacent layers of different thickness.[24,35,38]

The superior phase purity of our 2D perovskite films is expected to benefit device stability and to test this hypothesis, we performed stability measurements during operation of our $BA_2MA_3Pb_4I_{13}$ solar cell devices. The cells were encapsulated and subjected to a constant 1-Sun illumination for up to 800 hours – under 60±5 % relative humidity in air (Fig. 4e). The solar cells exhibit no "burn-in" effect[57] and lost less than 3% of their initial performances over 800 hours as measured using a standard AM 1.5G source. On the contrary, our control solar cell prepared with the classic synthesis method shows a burn-in effect and started to degrade after 200 hours. To the best of our knowledge, these stability results are better than state-of-art 2D perovskite devices with similar performances.[22,51,53] These results pave a path for achieving dominantly phase pure thin-films of 2D perovskites for realizing scalable, high-efficiency devices with long-term stability.

In summary, we developed a phase-selective synthesis method for fabricating 2D perovskite thin films with high phase purity, enhanced crystallinity and desired out-of-plane orientation. The *in-situ* characterization indicates the absence of an intermediate phase complex and reveals a seed assisted nucleation and film growth process. The presence of these sub-micron-sized seeds in the solution which preserves the memory of the dissolved single-crystals was verified. The films fabricated by this method resulted in photovoltaic devices with an efficiency of 17.1%, and enhanced stability.

Experimental section

2D perovskite parent crystal synthesis. The 2D perovskite parent crystals were synthesized by mixing PbI_2, MACl, and BAI (or 4AMPI in the case of the Dion Jacobson 2D perovskite) in appropriate ratios and dissolving these precursor materials in a mixture of HI/ H_3PO_2 according to

our previous reports.[[26,27]] The solution was stirred at high temperature (>190°C) until all the precursors were dissolved, then allowed to cool down to room temperature during which time crystals are formed. The crystallized 2D perovskite powder was separated, dried, and characterized using x-ray diffraction and absorption.

2D perovskite thin film synthesis. For the classic method, the precursors, BAI, MAI, and PbI_2 in appropriate ratios (with 5% of MACl additive) were dissolved in N, N dimethylformamide (DMF). The solution was stirred overnight in an argon filled glove box. Then, the precursor solution was spin coated on the substrates and annealed at 100℃ on a hot plate. In the phase-selective method, the parent crystals were dissolved in DMF with an addition of 5% MACl. After stirring the solution for at least 6 h, it was spin casted on the substrates followed by annealing at 100℃ on a hot plate. Detailed fabrication and solvent optimization techniques are presented in the method section of the Supplementary information.

In-situ X-Ray diffraction and absorption measurements. The precursor solutions were spin coated on glass substrates to obtain wet films and the samples were immediately transferred to the x-ray diffraction apparatus for measurements. The area of the diffraction peaks were monitored over time until the 2D perovskite films were fully formed. The same approach was used to probe the evolution of the optical density of the films during formation.

GIWAXS measurement and analysis. The GIWAXS patterns were measured at the Advanced Photon Source (8-ID-E) and the National Synchrotron Light Source-II (11-BM). At the beamline 8-ID-E, the 2D perovskite parent crystals and thin film samples were placed on a Linkam grazing incidence x-ray-scattering stage (temperature at 25°C) inside a vacuum chamber (10^{-4} torr) with the sample 228 mm away from a Pilatus 1M. The photon energy was 10.91 keV, and the beam size was 200 μm × 20 μm (H × V). At the beamline 11-BM, the samples were measured inside a

vacuum chamber (10^{-2} torr) with the sample 267mm away from a Pilatus 800K. The photon energy was 13.5 keV, and the beam size was 200 μm × 50 μm (H × V). All GIWAXS patterns were taken at 0.15° incident angle with typically 5 second exposure. The GIWAXS patterns were analyzed using the GIXSGUI package and Single Crystal-Crystal Maker software.[58]

In-situ microscopic imaging. Few microliters of the precursor solutions were drop casted on a thin microscopic slide that was then placed in a Titan microscope. The thin film formation without annealing was imaged using an oil immersion 100X objective over time by taking continuous snapshot images every second.

*Dynamic light scattering measurements***.** The precursor solutions were loaded into cylindrical glass cuvettes and the DLS correlation curves were collected at different angle with respect to the incident laser beam. The data were fitted using a single- or bi-exponential decay model to extract the size of the particles in the solution (see details in the method section of the Supplementary information).

Solar cell device fabrication. ITO glasses were cleaned by ultra-sonication in soap water, distilled water, acetone, acetone/ethanol (50:50) and isopropyl alcohol for 15 min each, followed by UV treatment for 30 minutes. A thin layer of PEDOT: PSS or NiO_x was spin-coated on the ITO substrates at 5,000 rpm for 30 seconds to form the hole-transporting layer. The coated substrates were then transferred to an argon-filled glovebox where the 2D perovskite thin films were synthetized by spin coating and annealing at 100℃for 10 min. The assemblies were completed by spin-coating (at 1,000 rpm for 300 seconds) a thin layer of PCBM (electron-transporting layer) and depositing on top aluminum contacts using a thermal evaporator with a shadow mask having a working area of 31.4 mm^2.

Solar cell Characterization. The solar cells were characterized by measuring the current–voltage curves while the cells are exposed to the light from a Newport ABB solar simulator (AM 1.5 G light). The external quantum efficiencies were collected by illuminating the device using the monochromatic light obtained from a quartz-tungsten-halogen source modulated at 2 kHz. The obtained photocurrent was measured by a lock-in amplifier. For stability measurements, the perovskite devices were encapsulated with a UV- curable epoxy and tested under open-circuit conditions, under full-spectrum simulated AM 1.5G in air using the same ABB solar simulator (following the ISOS-L protocol). The relative humidity was measured to be constant at 60±5 %RH.

Supporting Information

Supporting Information is available from the Wiley Online Library or from the author.

Acknowledgements

The work at Rice University was supported by the DOE-EERE 2022-1652 program. J.E. acknowledges the financial support from the Institut Universitaire de France. This work was supported by the Office of Naval Research (ONR) under grant N00014-20-1-2725. This research used facilities of the Advanced Photon Source, a U.S Department of Energy (DOE) Office of Science User Facility operated for the DOE Office of Science by Argonne National Laboratory under Contrast No. DE- AC02- 06CH11357. This research used the beamline 11-BM of the National Synchrotron Light Source II, a U.S. Department of Energy (DOE) Office of Science user facility operated for the DOE Office of Science by Brookhaven National Laboratory under Contract No. DE-SC0012704. W. Li, and M. H. K. Samani contributed equally to this work.

Competing interests: The authors declare no competing interests.

References

[1] M. Majidian, C. Grimaldi, L. Forró, A. Magrez, *Sci. Rep.* **2017**, *7*, 1.
[2] B. Sun, M. Vafaie, L. Levina, M. Wei, Y. Dong, Y. Gao, H. T. Kung, M. Biondi, A. H. Proppe, B. Chen, *Nano Lett.* **2020**, *20*, 3694.
[3] H. Wang, Z. Zeng, P. Xu, L. Li, G. Zeng, R. Xiao, Z. Tang, D. Huang, L. Tang, C. Lai, *Chem. Soc. Rev.* **2019**, *48*, 488.
[4] N. Wang, L. Cheng, R. Ge, S. Zhang, Y. Miao, W. Zou, C. Yi, Y. Sun, Y. Cao, R. Yang, *Nat. Photonics* **2016**, *10*, 699.
[5] D. Zhitomirsky, I. J. Kramer, A. J. Labelle, A. Fischer, R. Debnath, J. Pan, O. M. Bakr, E. H. Sargent, *Nano Lett.* **2012**, *12*, 1007.
[6] M. S. Arnold, J. L. Blackburn, J. J. Crochet, S. K. Doorn, J. G. Duque, A. Mohite, H. Telg, *Phys. Chem. Chem. Phys.* **2013**, *15*, 14896.
[7] T. Ishihara, J. Takahashi, T. Goto, *Phys. Rev. B* **1990**, *42*, 11099.
[8] D. B. Mitzi, C. A. Feild, W. T. A. Harrison, A. M. Guloy, *Nature* **1994**, *369*, 467.
[9] G. C. Papavassiliou, I. B. Koutselas, *Synth. Met.* **1995**, *71*, 1713.
[10] B. Saparov, D. B. Mitzi, *Chem. Rev.* **2016**, *116*, 4558.
[11] L. Mao, C. C. Stoumpos, M. G. Kanatzidis, *J. Am. Chem. Soc.* **2019**, *141*, 1171.
[12] J.-C. Blancon, A. V. Stier, H. Tsai, W. Nie, C. C. Stoumpos, B. Traoré, L. Pedesseau, M. Kepenekian, F. Katsutani, G. T. Noe, J. Kono, S. Tretiak, S. A. Crooker, C. Katan, M. G. Kanatzidis, J. J. Crochet, J. Even, A. D. Mohite, *Nat. Commun.* **2018**, *9*, 2254.
[13] X. Gong, O. Voznyy, A. Jain, W. Liu, R. Sabatini, Z. Piontkowski, G. Walters, G. Bappi, S. Nokhrin, O. Bushuyev, M. Yuan, R. Comin, D. McCamant, S. O. Kelley, E. H. Sargent, *Nat. Mater.* **2018**, *17*, 550.
[14] G. Long, R. Sabatini, M. I. Saidaminov, G. Lakhwani, A. Rasmita, X. Liu, E. H. Sargent, W. Gao, *Nat. Rev. Mater.* **2020**, *5*, 423.
[15] K. Leng, W. Fu, Y. Liu, M. Chhowalla, K. P. Loh, *Nat. Rev. Mater.* **2020**, 1.
[16] C. R. Kagan, D. B. Mitzi, C. D. Dimitrakopoulos, *Science* **1999**, *286*, 945.
[17] M. Yuan, L. N. Quan, R. Comin, G. Walters, R. Sabatini, O. Voznyy, S. Hoogland, Y. Zhao, E. M. Beauregard, P. Kanjanaboos, Z. Lu, D. H. Kim, E. H. Sargent, *Nat. Nanotechnol.* **2016**, *11*, 872.
[18] H. Tsai, W. Nie, J.-C. Blancon, C. C. Stoumpos, R. Asadpour, B. Harutyunyan, A. J. Neukirch, R. Verduzco, J. J. Crochet, S. Tretiak, others, *Nature* **2016**, *536*, 312.
[19] Z. Wang, Q. Lin, F. P. Chmiel, N. Sakai, L. M. Herz, H. J. Snaith, *Nat. Energy* **2017**, *2*, 1.
[20] B. Zhao, S. Bai, V. Kim, R. Lamboll, R. Shivanna, F. Auras, J. M. Richter, L. Yang, L. Dai, M. Alsari, X.-J. She, L. Liang, J. Zhang, S. Lilliu, P. Gao, H. J. Snaith, J. Wang, N. C. Greenham, R. H. Friend, D. Di, *Nat. Photonics* **2018**, *12*, 783.
[21] M. D. Smith, H. I. Karunadasa, *Acc. Chem. Res.* **2018**, *51*, 619.
[22] T. Luo, Y. Zhang, Z. Xu, T. Niu, J. Wen, J. Lu, S. Jin, S. (Frank) Liu, K. Zhao, *Adv. Mater.* **2019**, *31*, 1903848.
[23] Q. Shang, Y. Wang, Y. Zhong, Y. Mi, L. Qin, Y. Zhao, X. Qiu, X. Liu, Q. Zhang, *J. Phys. Chem. Lett.* **2017**, *8*, 4431.
[24] R. Quintero-Bermudez, A. Gold-Parker, A. H. Proppe, R. Munir, Z. Yang, S. O. Kelley, A. Amassian, M. F. Toney, E. H. Sargent, *Nat. Mater.* **2018**, *17*, 900.
[25] G. Grancini, M. K. Nazeeruddin, *Nat. Rev. Mater.* **2019**, *4*, 4.
[26] C. C. Stoumpos, D. H. Cao, D. J. Clark, J. Young, J. M. Rondinelli, J. I. Jang, J. T. Hupp, M. G. Kanatzidis, *Chem. Mater.* **2016**, *28*, 2852.

[27] L. Mao, W. Ke, L. Pedesseau, Y. Wu, C. Katan, J. Even, M. R. Wasielewski, C. C. Stoumpos, M. G. Kanatzidis, *J. Am. Chem. Soc.* **2018**, *140*, 3775.
[28] A. Krishna, S. Gottis, M. K. Nazeeruddin, F. Sauvage, *Adv. Funct. Mater.* **2019**, *29*, 1806482.
[29] P. Huang, S. Kazim, M. Wang, S. Ahmad, *ACS Energy Lett.* **2019**, *4*, 2960.
[30] Y.-K. Wang, D. Ma, F. Yuan, K. Singh, J. M. Pina, A. Johnston, Y. Dong, C. Zhou, B. Chen, B. Sun, H. Ebe, J. Fan, M.-J. Sun, Y. Gao, Z.-H. Lu, O. Voznyy, L.-S. Liao, E. H. Sargent, *Nat. Commun.* **2020**, *11*, 3674.
[31] M. Zhou, C. Fei, J. S. Sarmiento, H. Wang, *Sol. RRL* **2019**, *3*, 1800359.
[32] T. He, S. Li, Y. Jiang, C. Qin, M. Cui, L. Qiao, H. Xu, J. Yang, R. Long, H. Wang, M. Yuan, *Nat. Commun.* **2020**, *11*, 1672.
[33] Y. Han, S. Park, C. Kim, M. Lee, I. Hwang, *Nanoscale* **2019**, *11*, 3546.
[34] H. Tsai, W. Nie, J.-C. Blancon, C. C. Stoumpos, R. Asadpour, B. Harutyunyan, A. J. Neukirch, R. Verduzco, J. J. Crochet, S. Tretiak, L. Pedesseau, J. Even, M. A. Alam, G. Gupta, J. Lou, P. M. Ajayan, M. J. Bedzyk, M. G. Kanatzidis, A. D. Mohite, *Nature* **2016**, *536*, 312.
[35] N. R. Venkatesan, R. M. Kennard, R. A. DeCrescent, H. Nakayama, C. J. Dahlman, E. E. Perry, J. A. Schuller, M. L. Chabinyc, *Chem. Mater.* **2018**, *30*, 8615.
[36] Y. Lin, Y. Fang, J. Zhao, Y. Shao, S. J. Stuard, M. M. Nahid, H. Ade, Q. Wang, J. E. Shield, N. Zhou, A. M. Moran, J. Huang, *Nat. Commun.* **2019**, *10*, 1008.
[37] J.-C. Blancon, H. Tsai, W. Nie, C. C. Stoumpos, L. Pedesseau, C. Katan, M. Kepenekian, C. M. M. Soe, K. Appavoo, M. Y. Sfeir, S. Tretiak, P. M. Ajayan, M. G. Kanatzidis, J. Even, J. J. Crochet, A. D. Mohite, *Science* **2017**, *355*, 1288.
[38] M. Kepenekian, B. Traore, J.-C. Blancon, L. Pedesseau, H. Tsai, W. Nie, C. C. Stoumpos, M. G. Kanatzidis, J. Even, A. D. Mohite, S. Tretiak, C. Katan, *Nano Lett.* **2018**, *18*, 5603.
[39] A. Raja, L. Waldecker, J. Zipfel, Y. Cho, S. Brem, J. D. Ziegler, M. Kulig, T. Taniguchi, K. Watanabe, E. Malic, T. F. Heinz, T. C. Berkelbach, A. Chernikov, *Nat. Nanotechnol.* **2019**, *14*, 832.
[40] L. Liu, Y. Bai, X. Zhang, Y. Shang, C. Wang, H. Wang, C. Zhu, C. Hu, J. Wu, H. Zhou, Y. Li, S. Yang, Z. Ning, Q. Chen, *Angew. Chem. Int. Ed.* **2020**, *59*, 5979.
[41] C. M. M. Soe, G. P. Nagabhushana, R. Shivaramaiah, H. Tsai, W. Nie, J.-C. Blancon, F. Melkonyan, D. H. Cao, B. Traoré, L. Pedesseau, M. Kepenekian, C. Katan, J. Even, T. J. Marks, A. Navrotsky, A. D. Mohite, C. C. Stoumpos, M. G. Kanatzidis, *Proc. Natl. Acad. Sci.* **2019**, *116*, 58.
[42] L. N. Quan, M. Yuan, R. Comin, O. Voznyy, E. M. Beauregard, S. Hoogland, A. Buin, A. R. Kirmani, K. Zhao, A. Amassian, D. H. Kim, E. H. Sargent, *J. Am. Chem. Soc.* **2016**, *138*, 2649.
[43] B. Song, J. Hou, H. Wang, S. Sidhik, J. Miao, H. Gu, H. Zhang, S. Liu, Z. Fakhraai, J. Even, *ACS Mater. Lett.* **2020**, *3*, 148.
[44] Y. Zhao, H. Tan, H. Yuan, Z. Yang, J. Z. Fan, J. Kim, O. Voznyy, X. Gong, L. N. Quan, C. S. Tan, J. Hofkens, D. Yu, Q. Zhao, E. H. Sargent, *Nat. Commun.* **2018**, *9*, 1607.
[45] H.-J. Yen, P.-W. Liang, C.-C. Chueh, Z. Yang, A. K.-Y. Jen, H.-L. Wang, *ACS Appl. Mater. Interfaces* **2016**, *8*, 14513.
[46] A. Z. Chen, M. Shiu, J. H. Ma, M. R. Alpert, D. Zhang, B. J. Foley, D.-M. Smilgies, S.-H. Lee, J. J. Choi, *Nat. Commun.* **2018**, *9*, 1336.
[47] J. Dong, S. Shao, S. Kahmann, A. J. Rommens, D. Hermida- Merino, G. H. ten Brink, M. A. Loi, G. Portale, *Adv. Funct. Mater.* **2020**, *30*, 2001294.

[48] F. Hao, C. C. Stoumpos, Z. Liu, R. P. H. Chang, M. G. Kanatzidis, *J. Am. Chem. Soc.* **2014**, *136*, 16411.
[49] X. Zhang, X. Ren, B. Liu, R. Munir, X. Zhu, D. Yang, J. Li, Y. Liu, D.-M. Smilgies, R. Li, Z. Yang, T. Niu, X. Wang, A. Amassian, K. Zhao, S. (Frank) Liu, *Energy Environ. Sci.* **2017**, *10*, 2095.
[50] W. Nie, H. Tsai, J.-C. Blancon, F. Liu, C. C. Stoumpos, B. Traore, M. Kepenekian, O. Durand, C. Katan, S. Tretiak, *Adv. Mater.* **2018**, *30*, 1703879.
[51] B.-E. Cohen, Y. Li, Q. Meng, L. Etgar, *Nano Lett.* **2019**, *19*, 2588.
[52] H. Li, X. Wang, T. Zhang, X. Gong, Q. Sun, H. Pan, Y. Shen, S. Ahmad, M. Wang, *Adv. Funct. Mater.* **2019**, *29*, 1903293.
[53] T. Niu, H. Ren, B. Wu, Y. Xia, X. Xie, Y. Yang, X. Gao, Y. Chen, W. Huang, *J. Phys. Chem. Lett.* **2019**, *10*, 2349.
[54] Y. Zheng, T. Niu, J. Qiu, L. Chao, B. Li, Y. Yang, Q. Li, C. Lin, X. Gao, C. Zhang, Y. Xia, Y. Chen, W. Huang, *Sol. RRL* **2019**, *3*, 1900090.
[55] F. Zhang, H. Lu, J. Tong, J. J. Berry, M. C. Beard, K. Zhu, *Energy Environ. Sci.* **2020**, *13*, 1154.
[56] H. Tsai, R. Asadpour, J.-C. Blancon, C. C. Stoumpos, J. Even, P. M. Ajayan, M. G. Kanatzidis, M. A. Alam, A. D. Mohite, W. Nie, *Nat. Commun.* **2018**, *9*, DOI 10.1038/s41467-018-04430-2.
[57] M. V. Khenkin, E. A. Katz, A. Abate, G. Bardizza, J. J. Berry, C. Brabec, F. Brunetti, V. Bulović, Q. Burlingame, A. D. Carlo, R. Cheacharoen, Y.-B. Cheng, A. Colsmann, S. Cros, K. Domanski, M. Dusza, C. J. Fell, S. R. Forrest, Y. Galagan, D. D. Girolamo, M. Grätzel, A. Hagfeldt, E. von Hauff, H. Hoppe, J. Kettle, H. Köbler, M. S. Leite, S. (Frank) Liu, Y.-L. Loo, J. M. Luther, C.-Q. Ma, M. Madsen, M. Manceau, M. Matheron, M. McGehee, R. Meitzner, M. K. Nazeeruddin, A. F. Nogueira, Ç. Odabaşı, A. Osherov, N.-G. Park, M. O. Reese, F. D. Rossi, M. Saliba, U. S. Schubert, H. J. Snaith, S. D. Stranks, W. Tress, P. A. Troshin, V. Turkovic, S. Veenstra, I. Visoly-Fisher, A. Walsh, T. Watson, H. Xie, R. Yıldırım, S. M. Zakeeruddin, K. Zhu, M. Lira-Cantu, *Nat. Energy* **2020**, *5*, 35.
[58] Z. Jiang, X. Li, J. Strzalka, M. Sprung, T. Sun, A. R. Sandy, S. Narayanan, D. R. Lee, J. Wang, *J. Synchrotron Radiat.* **2012**, *19*, 627.